Volumetric measurements of a self-similar adverse pressure gradient turbulent boundary layer using single-camera light-field particle image velocimetry

Zhao, Zhou; Buchner, Abel John; Atkinson, Callum; Shi, Shengxian; Soria, Julio

DOI
10.1007/s00348-019-2788-0

Publication date
2019

Document Version
Final published version

Published in
Experiments in Fluids

Citation (APA)
Zhao, Z., Buchner, A. J., Atkinson, C., Shi, S., & Soria, J. (2019). Volumetric measurements of a self-similar adverse pressure gradient turbulent boundary layer using single-camera light-field particle image velocimetry. *Experiments in Fluids*, *60*(9), Article 141. https://doi.org/10.1007/s00348-019-2788-0

Experiments in Fluids (2019) 60:141
https://doi.org/10.1007/s00348-019-2788-0

RESEARCH ARTICLE

Volumetric measurements of a self-similar adverse pressure gradient turbulent boundary layer using single-camera light-field particle image velocimetry

Zhou Zhao[1] · Abel-John Buchner[2,3] · Callum Atkinson[2] · Shengxian Shi[1] · Julio Soria[2]

Received: 29 April 2019 / Revised: 9 July 2019 / Accepted: 3 August 2019 / Published online: 13 August 2019

Abstract

As a novel volumetric particle image velocimetry technique, single-camera light-field PIV (LF-PIV) is able to acquire three-dimensional flow fields through a single camera. Compared with other multi-camera 3D PIV techniques, LF-PIV has distinct advantages, including concise hardware setup and low optical access requirements. Its capability has proven effective in many experimental investigations. In this study, the use of LF-PIV in measuring a self-similar adverse pressure-gradient turbulent boundary layer (APG-TBL) is demonstrated. Experiments are performed in a large water tunnel at the Laboratory for Turbulence Research in Aerospace and Combustion (LTRAC), Monash University. Sets of 250 light-field PIV image pairs are captured covering both the inner and outer regions of the boundary layer. Instantaneous 3D velocity fields are reconstructed using a GPU accelerated density ray tracing multiplicative reconstruction technique (DRT-MART) and three-dimensional cross-correlation methods. The LF-PIV results are compared with two-dimensional PIV (2D-PIV) measurements of the same flow. Comparable accuracy to 2D-PIV is achieved for first- and second-order velocity statistics above approximately $y/\delta_1 = 1$.

Electronic supplementary material The online version of this article (https://doi.org/10.1007/s00348-019-2788-0) contains supplementary material, which is available to authorized users.

✉ Shengxian Shi
kirinshi@sjtu.edu.cn

✉ Julio Soria
julio.soria@monash.edu

[1] School of Mechanical Engineering, Shanghai Jiao Tong University, Shanghai 200240, China

[2] Laboratory for Turbulence Research in Aerospace and Combustion, Department of Mechanical and Aerospace Engineering, Monash University, Clayton 3800, Australia

[3] Laboratory for Aero and Hydrodynamics, Faculty of Mechanical, Maritime, and Materials Engineering, Delft University of Technology, Delft, The Netherlands

Graphic abstract

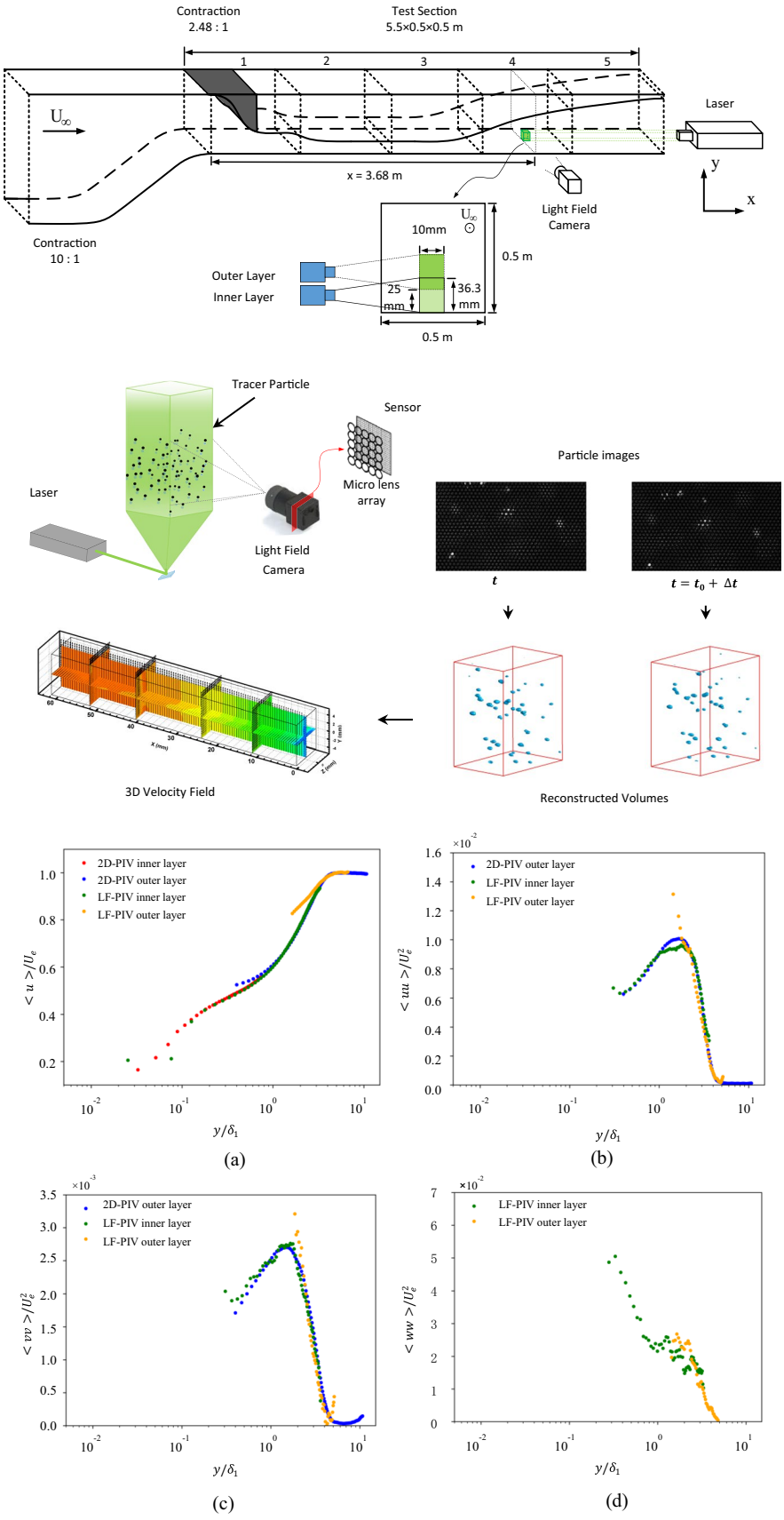

1 Introduction

Particle image velocimetry (PIV) has advanced greatly over the past several decades. It has evolved from a relatively restrictive two-component two-dimensional (2C-2D) measurement technique into a valuable tool capable of extracting volumetric, time-resolved, flow information. Three-component three-dimensional (3C-3D) information has been successfully retrieved by adapting the basic PIV principle in a variety of ways, including: defocusing digital PIV (DDPIV, Willert and Gharib 1992; Pereira et al. 2000), holographic PIV (HPIV, Hinsch 2002; Katz and Sheng 2010), tomographic PIV (Tomo-PIV, Elsinga et al. 2006; Atkinson and Soria 2009; Scarano 2013), and synthetic aperture PIV (SAPIV, Belden et al. 2010). These volumetric PIV techniques can fully acquire the volumetric 3C-3D velocity field, allowing unprecedented insight into the three-dimensional structure of a variety of complex flows and its effect on, for example, flow stability (Buchner et al. 2017) or momentum transport (Buchner et al. 2016) which drive evolution in these flows. This is a significant improvement over previous efforts, such as stereoscopic PIV (stereo PIV, Prasad and Adrian 1993) which yields three-dimensional velocity but only in two-dimensional space, or scanning PIV (Brucker 1996) which is not a truly instantaneous representation of the three-dimensional flow. One of the earlier efforts at extracting 3D information from flows, DDPIV, recovers the volumetric information from defocused particle images, and usually uses a triple-camera setup to ensure a sufficient accuracy. DDPIV is generally constrained to a small measurement volume and very sparse seeding density. HPIV, which resolves volumetric velocity fields from particle holograms, is considered as the first truly 3C-3D flow measurement technique; however, its widespread application is limited by the need for a rather complex optical setup. A more widely applied volumetric PIV technique is Tomo-PIV, which employs multiple view geometry method (typically with 4–8 cameras) to capture particle images and obtain 3C-3D velocity fields through multiplicative reconstruction (MART) of a three-dimensional intensity field and subsequent three-dimensional cross correlation. It can be performed at much higher seeding density and, thus, achieve higher spatial resolution within a relatively large measurable volume than the other aforementioned volumetric measurement techniques. However, the requirement for multiple optical access paths practically limits the application of Tomo-PIV in many space-constrained situations (Chen and Sick 2017). Besides, the use of a multi-camera system requires accurate calibration which is prone to environmental disturbances, e.g., vibrations in the high-speed wind tunnel and rotary turbomachinery tests. Reconstruction algorithms such as MART which rely on multiple-view geometry are particularly sensitive to calibration errors which, if larger the particle image diameter, can cause the reconstruction to rapidly degrade in quality and fail. Similar difficulties are also faced by the SAPIV, which uses a large camera array (normally 8–15 cameras) to get the volumetric velocity field. The benefit in developing single-camera techniques is thus clear.

The recently developed single-camera light-field PIV (LF-PIV, Ding et al. 2015; Fahringer et al. 2015) technique records the three-dimensional information of particles with a single plenoptic camera, using a closely encapsulated microlens array (MLA) fixed near a high-resolution image sensor. Recent efforts analyzing key design features (Shi et al. 2016; Deem et al. 2016) and developing more efficient and higher-accuracy light-field reconstruction algorithms (Fahringer et al. 2015; Shi et al. 2017), have evinced that single-camera LF-PIV can achieve similar measurement accuracy to Tomo-PIV, when the pixel and MLA resolutions of the plenoptic camera are relatively high (Shi et al. 2018). Although LF-PIV has been successfully applied in many flow experiments (Li et al. 2017; Xu et al. 2017; Bolton et al. 2017; Ding et al. 2018), a canonical test revealing its performance in measuring wall-bounded turbulent flows remains absent.

Turbulent boundary layers play a significant role in a range of industrial, biological, and environmental flows, particularly in affecting the efficiency and performance of transportation and energy generation platforms. Those turbulent boundary layers influenced by an adverse pressure gradient are particularly salient due to their relationship with flow separation and all the practical consequences that have across a range of contexts. Turbulent boundary layers without a pressure gradient regularly serve as a canonical flow by which to study the physics of turbulence, but studies on adverse pressure-gradient turbulent boundary layers (APG-TBL) are complicated by the non-local effects of variation of pressure gradient along the flow direction. Self-similar APG-TBL's allow the study of the influence of a single non-dimensional pressure gradient over the coherent domain of boundary layer, and have, thus, recently been a topic of intense interest (e.g., Kitsios et al. 2016, 2017, Bobke et al. 2017; Vila et al. 2017; Eisfelder et al. 2018). Turbulent boundary layers are inherently three-dimensional, and so understanding the application of all available three-dimensional measurement techniques to these flows is imperative. While studies on APG-TBL is normally complicated by the non-linear variation of pressure gradient along the flow direction, a self-similar APG-TBL allows studying the influence of a single non-dimensional pressure gradient over the coherent domain of boundary layer. As such, the current study aims to apply the LF-PIV technique to a self-similar adverse pressure-gradient turbulent boundary layer to fully examine the performance of LF-PIV against benchmark

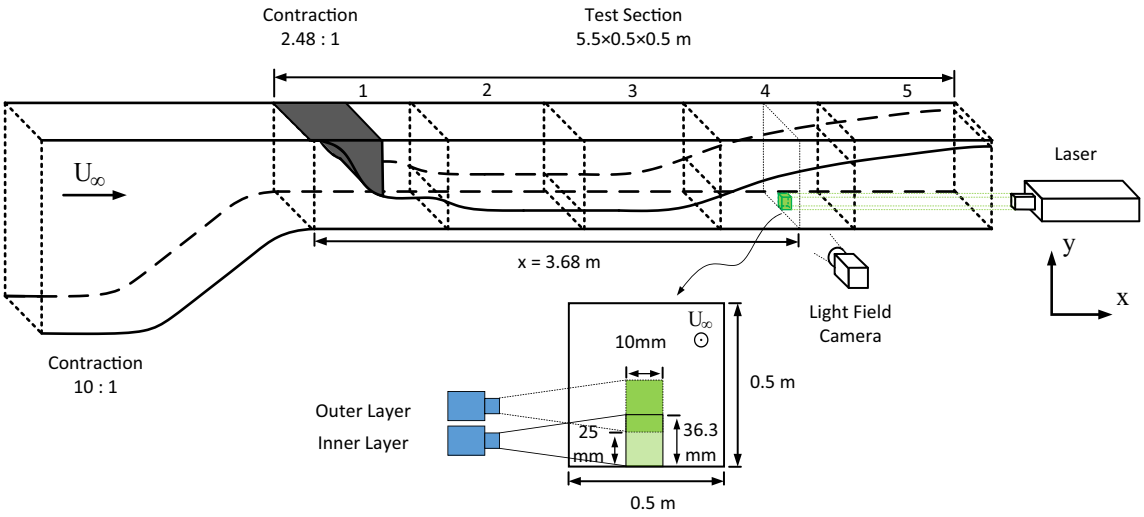

Fig. 1 Schematic of the LTRAC water tunnel and the LF-PIV experimental setup of the inner and outer layer measurements

results obtained for the same flow using two-dimensional planar PIV (2D-PIV).

This paper is structured as follows: In Sect. 2, the experimental arrangement will be described. The LF-PIV data processing procedure and the validation of the velocity field will be presented in Sect. 3, after which Sect. 4 will compare the statistical properties of the boundary layer as measured by LF-PIV and compared with 2D-PIV. Finally, Sect. 5 will summarize and suggest possible variations to the technique which could help to improve measurement accuracy in the future. We note that a shorter version of this paper was previously presented at a conference (Zhao et al. 2018). Our initial conference paper did not address the problem of resolution variation in the z-direction. This manuscript addresses this issue and provides additional analysis on resolution variation and more careful validation of data by using the velocity field divergence, with more velocity fields.

2 Experiment

An APG-TBL was formed in the $0.5 \times 0.5 \times 5.5$ m water tunnel at the Laboratory for Turbulence Research in Aerospace and Combustion (LTRAC), Monash University. This facility was modified by inserting an extra contraction at the upstream end of the test section and a flexible polycarbonate roof in the remaining length of this section. This roof could be adjusted via a series of threaded supporting rods, thus forming a variable area test section. A false floor was constructed of glass and anodized aluminum and was inserted into the test section to provide a consistently flat surface, where the boundary layer measurements can be performed without any curvature effects. The flexible roof's position was iteratively adjusted according to statistical profiles obtained virtually instantaneously from an accelerated PIV analysis procedure (Atkinson et al. 2015), so as to establish the desired pressure gradient. This procedure involved measuring the boundary layer at multiple streamwise locations and real-time processing the images using an in-house image acquisition and PIV analysis algorithm. Previous work on the water tunnel design and experimental validation of the generated boundary layer (Atkinson et al. 2015, 2016a) indicated that a self-similar APG-TBL could reliably be established under a moderate adverse pressure gradient on the false floor in the fourth test section (see Fig. 1) over nine boundary layer thicknesses in the streamwise direction. Here, the dimensionless adverse pressure gradient was set to $\beta = \left(\delta_1/\tau_w\right) \cdot \mathrm{d}P/\mathrm{d}x = 2.0 \pm 0.15$, where $\mathrm{d}P/\mathrm{d}x$ is the streamwise dimensional pressure gradient, δ_1 the displacement thickness of the boundary layer, and τ_w is the local mean wall shear stress. The mean external velocity, U_∞, in the self-similar region was approximately 440–470 mm/s (Atkinson et al. 2016b), and the Reynolds number at the upstream end of this region was $Re_{\delta_1} \approx 5400$.

Table 1 Key parameters of the 2D-PIV measurement

Spatial resolution	47.1 μm/pixel
Magnification	0.14
F-stop, $f^\#$	8
Measurement domain	$0 \le y/\delta_1 \le 10$
Exposure	0.3 ms
Acquisition frequency	500 Hz
Interrogation window $\mathrm{IW}_x \times \mathrm{IW}_y$ (initial)	96 × 64 pixels
Interrogation window $\mathrm{IW}_x \times \mathrm{IW}_y$ (final)	64 × 24 pixels
Vector spacing	$\Delta y = 16$ pixels

2.1 Benchmark 2D-PIV measurement

A 2D-PIV experiment to measure the properties and self-similarity of the APG-TBL and to provide a validation dataset for the LF-PIV experiment was performed at several streamwise locations, from $x = 3.68$ to $x = 4.18$ m (over approximately 9δ) at intervals differing by 100 mm. An ILA sCMOS camera with 6.5 µm pixel size was used, at a spatial resolution of 47.1 µm/pixel. Only a narrow measurement domain measuring 96 pixels in the streamwise direction was used, providing a local velocity profile only. The full 2560 pixel resolution of each camera was employed in the wall-normal y-direction. By cropping the sensor, this also allowed us to run the cameras at a high frame rate. This narrow measurement domain was illuminated by an Oxxius Slim 532 nm 226 mW continuous wave laser, with a light sheet width of approximately 1 mm. The 0.3 ms exposure time of the camera was sufficiently short to provide "frozen" images of the 11 µm diameter hollow glass spheres (Potters) used as seeding in this experiment.

Planar two-component, two-dimensional (2C-2D) PIV was performed using these images, by way of a multigrid PIV cross correlation (Soria 1996). Initial and final interrogation window sizes are given in Table 1. A wall-normal vector spacing of $\Delta y = 16$ pixels ($0.012\ \delta$) was obtained. A second, spatial resolution 12.9 µm/pixel, measurement of the near-wall region was used to obtain a mean streamwise velocity profile down to within the viscous sublayer through ensemble-averaged cross-correlation single-pixel resolution PIV. It is from this measurement that the wall shear stress, τ_w, could be calculated and an accurate dimensionless streamwise pressure gradient, β, could be computed. The first- and second-order statistics at each y-location in the outer measurement were calculated from a total of 30,000 samples, although the high frame rate relative to the eddy turnover time, $t_e = \delta_1/U_e \approx 23$ ms, means that the independent sample size is closer to 2500. Table 1 lists the key parameters relating to the camera acquisition and 2D-PIV analysis setup.

2.2 LF-PIV measurement

The use of the LF-PIV technique is, here, demonstrated in measuring this APG-TBL. The experimental arrangement for LF-PIV is illustrated in Fig. 1. To evaluate its performance compared with 2D-PIV, the light-field camera measurement was performed at the beginning of the self-similar region, at $x = 3.68$ m downstream of the tunnel entrance, focusing on the tunnel center plane. The water tunnel was homogenously seeded with approximately neutrally buoyant

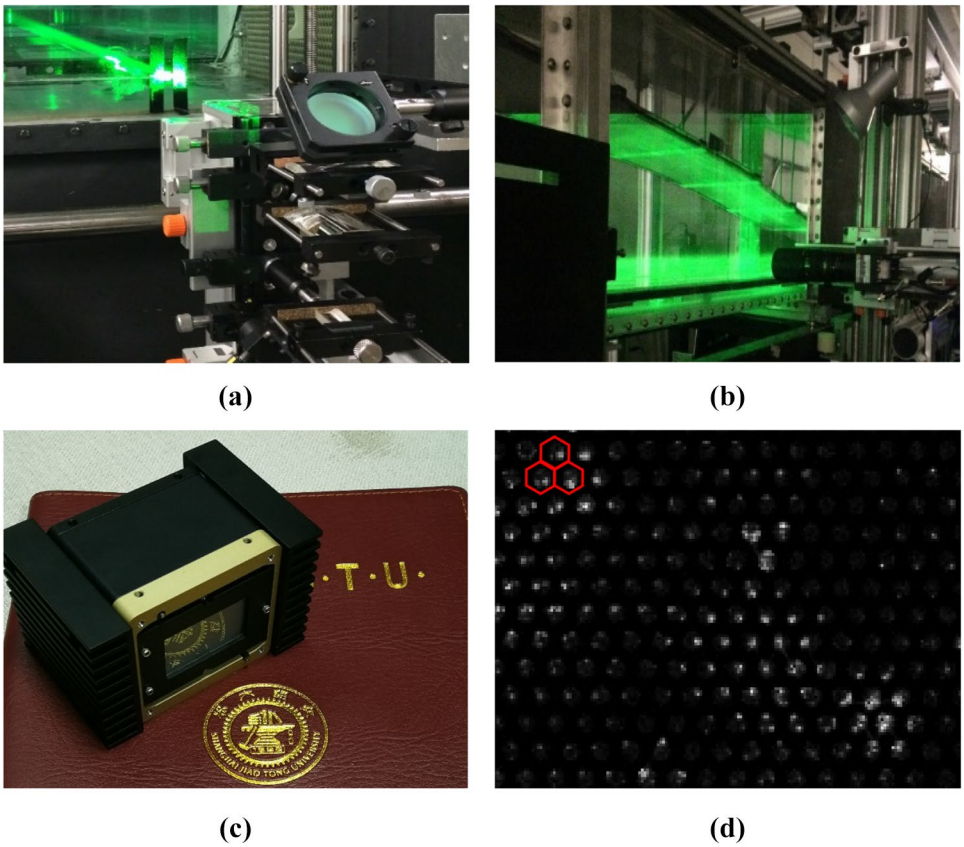

Fig. 2 **a** Experimental setup of the laser path. **b** Experimental setup of the LF-PIV system. **c** In-house 29 M pixel light-field camera. **d** Partially magnified particle image. The red hexagonal frame in the upper left corner indicates the arrangement of the microlens array, with each cell containing the sub-image formed by a single microlens

Table 2 Key parameters of the LF-PIV experiment

Pixel resolution	6600 × 2200
Pixel size	5.5 µm
MLA resolution	520 × 180
Lenslet size	70 µm
Lenslet focal length	300 µm
Magnification	~ 1
Test volume	61.3 × 12.8 × 10 mm
Light sheet thickness	~ 12 mm
Particle density	~ 0.5 ppm (particle per microlens)
Particle size	11 µm
Capture frequency	1 Hz
Interframe time	0.6 ms

hollow glass spheres (Potters, 11 µm). A test volume measuring $61.3 \times 12.8 \times 10$ mm^3 was uniformly illuminated by a double pulse Nd:YAG laser (Gemini PIV 15, 90 mJ/pulse, 532 nm). The laser beam was spread into a volume using two cylindrical lenses and entered the tunnel from the end of section 5 along the x-direction (Fig. 2a, b), so that the reflections from the false floor were minimized. Measurements were taken at 1 Hz so that subsequent velocity fields were statistically independent of one another. The interframe time between each laser pulse of $\Delta t = 0.6$ ms. The particle image pairs were recorded using an in-house 29 M pixel light-field camera fitted with a Micro-NIKKOR 200 mm lens (Fig. 2c). This light-field camera contains a 520×360 microlens array near the high-resolution image sensor (ImperX B6640). The design and evaluation of a similar camera's performance are detailed in Shi et al. (2016, 2018).

To achieve the best accuracy, the magnification of light-field camera was set to $M = 1$ (Shi et al. 2016), which did not permit to capture the flow across the whole boundary layer thickness in a single measurement. Due to this limit, the measurement was separated in into two: One series of measurements to capture the near-wall region, and another for the outer part of the boundary layer wherein the camera was shifted upwards from the wall by 25 mm. The statistics obtained from each of these experiments were subsequently stitched by interpolation onto a common grid. 600 independent light-field PIV image pairs were captured and processed for each of the inner and outer layer measurements (Table 2).

3 Data processing of LF-PIV

3.1 Velocity field data

LF-PIV measurements consist of illuminating a seeded flow in the same manner as in traditional PIV, with the exception that the camera has been fitted with a microlens array (MLA). In using an MLA, particle images are scattered on the camera sensor, contributing light over a region of pixels. From this scattered information, three-dimensional intensity volumes can be reconstructed, with subsequent volumetric cross correlation yielding instantaneous

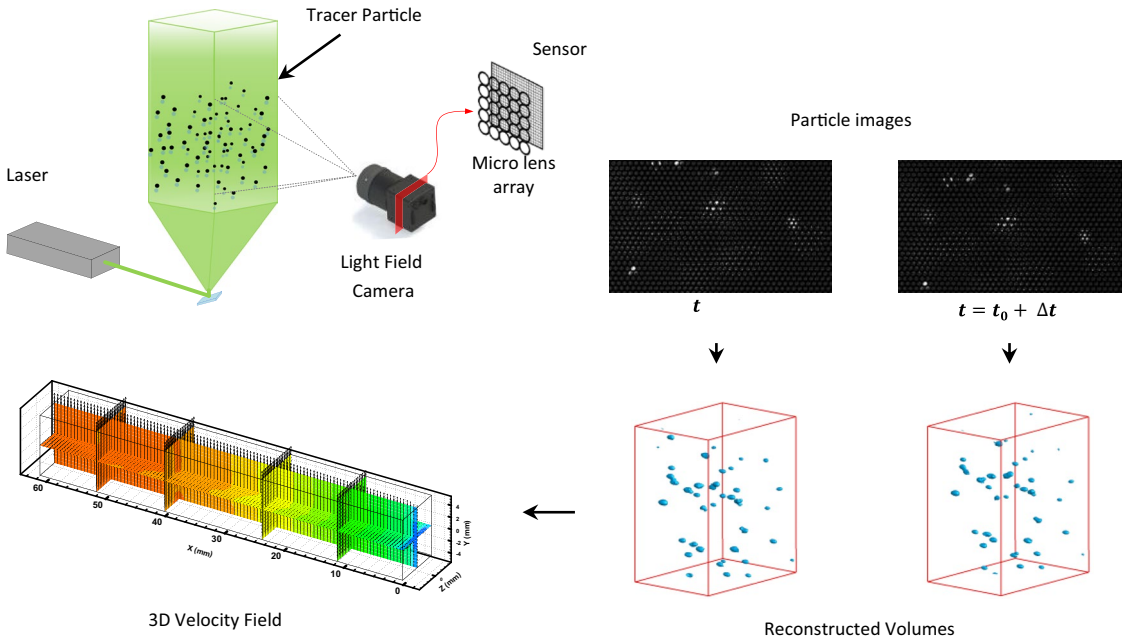

Fig. 3 Schematic diagram of the LF-PIV workflow, indicating acquisition of images using a plenoptic camera fitted with microlens array (MLA); for example, real particle image pair as viewed through the MLA-fitted camera, isosurfaces of intensity within the reconstructed volumetric domain, and the resulting three-dimensional velocity field

velocity fields. Figure 3 conceptually outlines the workflow required for an LF-PIV experiment. In addition, calibration of the camera, and some image preprocessing, may be performed prior to volume reconstruction, and some data validation applied after determination of vectors via cross correlation. The algorithms and procedures necessary to perform this analysis have previously been developed and described in detail in several papers (Fahringer et al. 2015; Shi et al. 2016, 2017). A full explanation of the theory of LF-PIV lies beyond the scope of this paper, but a flowchart of the LF-PIV procedure is given in Fig. 4, with key references as a guide for the reader.

In the light-field algorithm, as implemented here, the light-field particle images (Fig. 2d) were reconstructed by the Dense Ray Tracing-based MART (DRT-MART) method (Shi et al. 2017). The main steps are: first, a dense ray tracing method is used to identify non-zero voxels and calculate the weighting coefficients mapping the relationship between the identified voxel and influenced pixels. Then the MART algorithm (Herman and Lent 1976) is used to iteratively update the intensity of each voxel, as per Eq. 1.

$$E\left(X_j, Y_j, Z_j\right)^{k+1} = E\left(X_j, Y_j, Z_j\right)^{k} \left(\frac{I\left(x_i, y_i\right)}{\sum_{j \in N_i} w_{i,j} E\left(X_j, Y_j, Z_j\right)^{k}} \right)^{\mu w_{i,j}}, \quad (1)$$

where $E\left(X_j, Y_j, Z_j\right)$ is the intensity of the jth voxel; $I\left(x_i, y_i\right)$ the intensity of the ith pixel, which is known from the captured light-field image; and $w_{i,j}$ is the weighting coefficient, which is the contribution of light intensity from the jth voxel to the ith pixel value. μ is a scalar relaxation parameter. Numerical simulation and experimental validation have shown that the DRT-MART reconstruction algorithm can achieve similar reconstruction accuracy to Tomo-PIV when high-resolution image sensor and microlens array are utilized (Shi et al. 2018).

In this experiment, the raw particle images were reconstructed by the DRT-MART method with a pixel-to-voxel ratio of 3:3:10 in x-, y- and z-directions, respectively, where the z-direction is defined along the camera viewing axis. This results in a reconstruction domain of $733 \times 2200 \times 182$ voxels and spatial resolution of $0.0165 \times 0.0165 \times 0.055$ mm^3/voxel. The raw instantaneous velocity volumes were calculated by three-dimensional multi-grid cross correlation (Soria 1996) with 50% overlap and an initial and final interrogation window size of $256 \times 256 \times 64$ and $128 \times 128 \times 32$, respectively. After vector validation (described in Sect. 3.2), the resulting three-dimensional velocity fields have a resolution of $0.558 \times 0.637 \times 0.526$ mm^3/vector, for a total of 23,465 ($19 \times 65 \times 19$) velocity vectors per field. Reconstruction and cross correlation are computationally expensive and so were accelerated by GPU parallel computing to reduce processing time such that the reconstruction of each

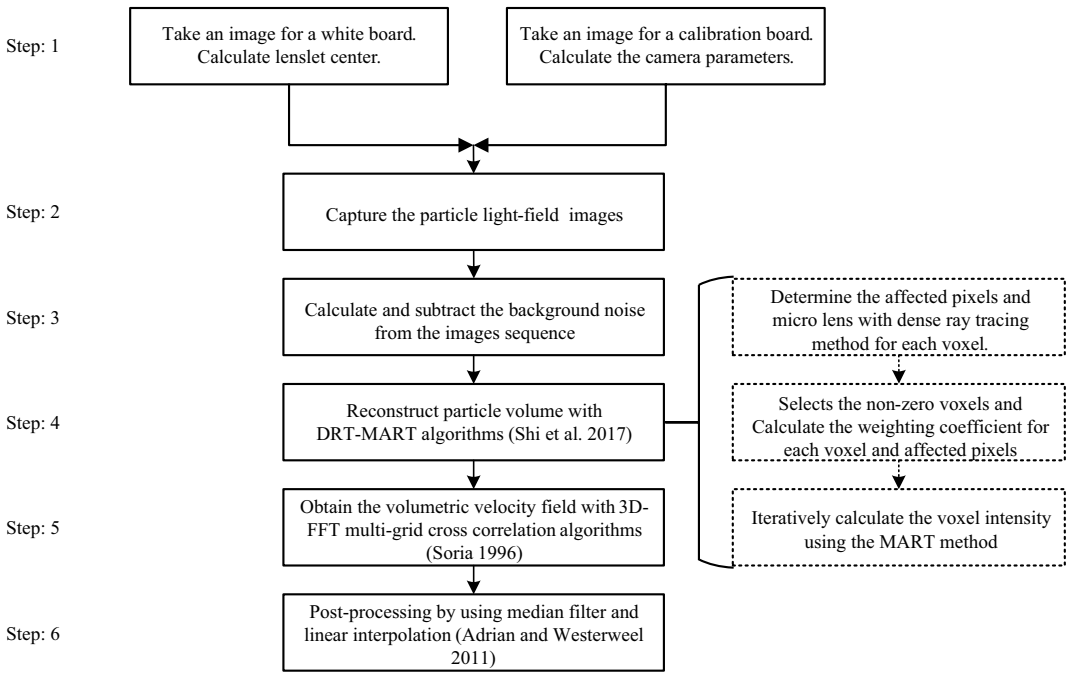

Fig. 4 Flowchart of the LF-PIV experimental and data analysis procedure. The sub-chart with dashed outlines indicates steps taken in the LF reconstruction algorithm

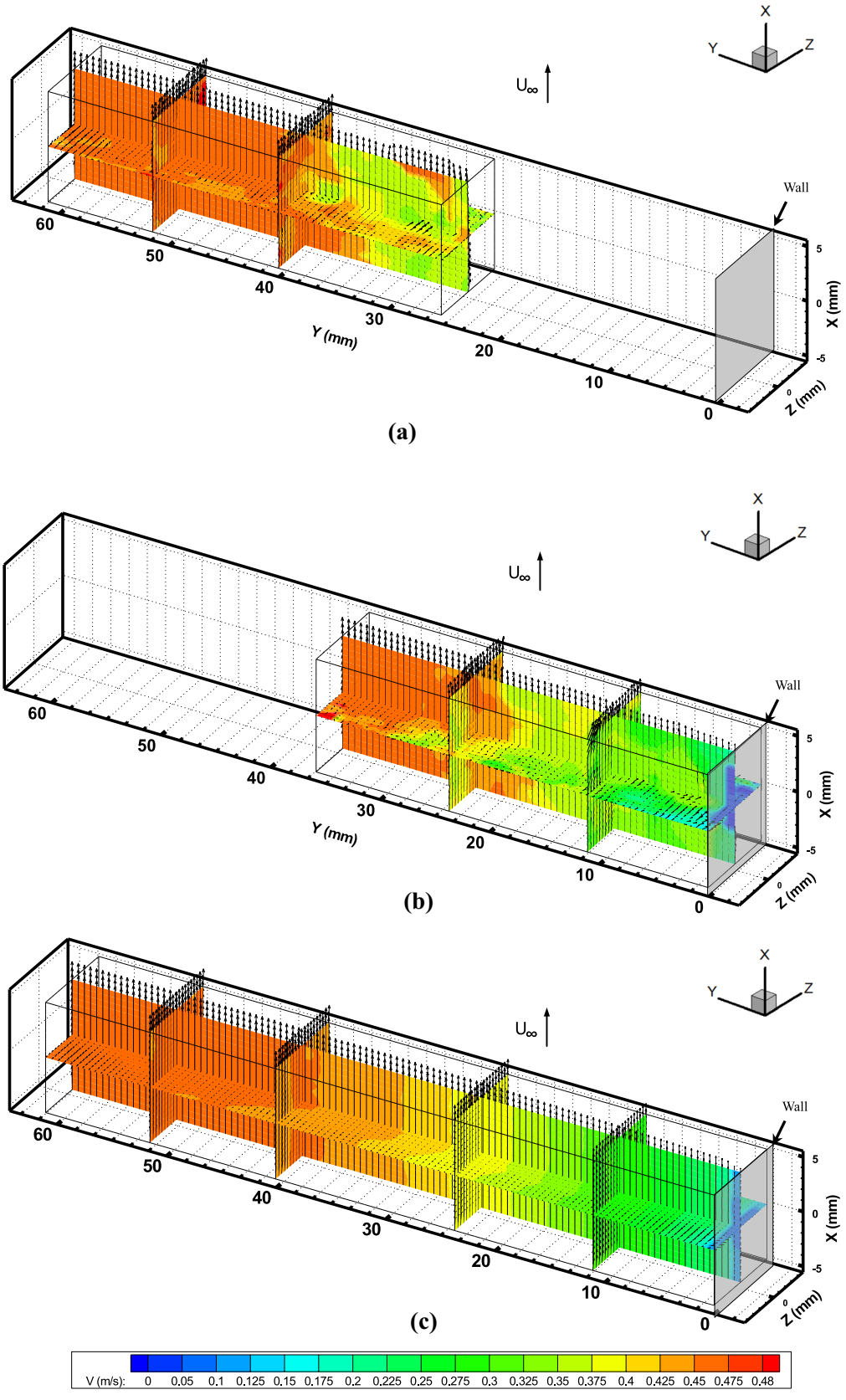
X
Y
Z
U∞
Wall
60
50
40
30
20
10
0
Y (mm)
5
0
-5
X (mm)
0
Z (mm)
(a)
(b)
(c)
V (m/s): 0 0.05 0.1 0.125 0.15 0.175 0.2 0.225 0.25 0.275 0.3 0.325 0.35 0.375 0.4 0.425 0.45 0.475 0.48

◂**Fig. 5** An example instantaneous velocity field from **a** the outer layer measurements, and **b** the inner layer measurements; **c** average volumetric velocity field of the entire APG-TBL stitched together from inner and outer region LF-PIV measurements. The outer flow is in the positive x-direction, and the wall lies here on the right-hand side of the figure

three-dimensional particle distribution map takes $\sim O(150)$ min, and each instantaneous velocity field obtained by three-dimensional cross correlation takes approximately 15 min. Six GeForce 1080Ti graphics cards were used to calculate 600 pairs of 3D transient velocity fields for each of the inner and outer layer measurements.

An example instantaneous velocity field from each of the inner and outer measurement domains is given in Fig. 5a, b. This demonstrates the extent and overlap of the domains, and the fluctuating nature of the flow. In the slices provided in these figures, turbulent three-dimensional structure is clearly visible, information that is not available from 2D techniques, and which is much more easily obtained with the single-camera LF-PIV technique than from other multi-camera techniques such as Tomo-PIV.

3.2 Validation of the LF-PIV velocity field data

Figure 5c shows the average flow field obtained from the entire measurement set of 600 velocity fields, with inner and outer camera measurements stitched together. The measurement volume extends 10 mm in the spanwise (z-) direction and 12.8 mm in the streamwise (x-) direction. The flow is statistically homogeneous in z, and over the streamwise (x-) extent of the measurement domain grows minimally. We are, therefore, justified in calculating statistical properties from all available data at each wall-normal y-location, thus increasing the effective sample size in calculating statistical profiles. So, the statistics in each y-location are accumulated from a total of 600 statistically independent sets consisting of 361 samples each.

The uncertainty in the estimate of the mean quantities was determined based on the independent sample size, N, as a 95% confidence interval equal to 1.96 times the standard error which converges with sample size as $\mathrm{SE}(\langle u \rangle) = \sqrt{\langle uu \rangle / N}$. The uncertainty of the mean velocity profile peaks, therefore, at approximately 0.02% of the freestream velocity. A 95% confidence interval on the sample-estimated Reynolds stress can, however, be ascertained from the Chi-squared test, as per Sheskin (2000), as ranging from -10.4% to $+12.4\%$ from the estimated value. This, however, does not account for the biasing effects of noise in the measurement. Errors on second-order statistics can be significant, as any noise in the measurement will increase the apparent magnitude of the Reynolds stresses, while the spatial filtering due to the low resolution of the measurement has the opposite effect.

Prior to statistical analysis, the validity of individual vectors is assessed by reference to their neighbors through the well-established median vector validation test of Adrian and Westerweel (2011). This resulted in approximately 2% of vectors being identified as likely erroneous. To increase the robustness of the statistical profile estimates, data were further validated through rejection of velocity outliers greater than 3 standard deviations from the mean value for each y-location. This led to a total of approximately 3% of the vectors being removed from the center region of the LF-PIV volumes, rising to 5–7% rejection rate near the edges due to the lower resolution and higher noise in those regions.

Since three-dimensional data are available, the accuracy of the velocity fields can be directly assessed by examining the divergence and recognizing the incompressibility of this APG-TBL flow. Figure 6 presents joint probability density functions (JPDFs) comparing the spanwise velocity gradient against the sum of the streamwise and wall-normal velocity gradients. The incompressibility of the flow demands that the continuity equation should be satisfied, and thus for a perfect measurement all the samples would lie along the $-\partial w/\partial z = \partial u/\partial x + \partial v/\partial y$ line (red dashed line) on these plots.

The resolution of LF-PIV in the z-direction is worse than the x/y-direction, and uncertainty is higher, such that the $\partial w/\partial z$ component dominates in Fig. 6. Such results are consistent with previous findings that the spatial resolution of the light-field camera is non-uniform and the resolution of LF-PIV in the z-direction is lower than in the x- and y-direction (Shi et al. 2016; Deem et al. 2016). Generally, the overall distribution is concentrated symmetrically about the origin, $(0, 0)$, especially from the partially enlarged Fig. 6b, d. The extent of the JPDF is less in the x/y-direction than the z-direction, where it is elongated due to poor z-direction resolution. The ratio between the z-direction and the x/y-direction is about 10:1. This indicates that velocity gradients in the z-direction are much larger than the gradients in the other directions, contributing to erroneous non-zero divergence. The resolution of LF-PIV in the z-direction is poor, which is caused by the limited sampling rate in the z-direction of the light-field imaging. This limitation of the LF-PIV technique is more pronounced than in other volumetric PIV techniques, such as Tomo-PIV and holographic-PIV, and produces reconstructed particle shapes which are much longer in the viewing axis (z-direction) than in the other directions (Deem et al. 2016; Shi et al. 2017). Although the reconstruction volume was discretized with a pixel–voxel ratio of 3:1 in both x- and y-directions and 10:1 in the z-direction to reduce the error caused by the elongation effect, the JPDF shows that errors in the z-direction are still significant.

4 Velocity profiles compared with the 2D-PIV results

To further evaluate the measurement performance of LF-PIV, a direct comparison is performed against 2D-PIV measurement from a previous measurement campaign in the same facility (Atkinson et al. 2016a). To compare with the benchmark 2D-PIV results, statistical profiles were calculated from a streamwise-restricted segment of the volumetric LF-PIV data, assuming constant boundary layer properties over this restricted domain. The wall-normal profiles of the mean streamwise velocity $\langle u \rangle$ and Reynolds stress components $\langle uu \rangle$, $\langle vv \rangle$, $\langle uv \rangle$, $\langle ww \rangle$, normalized using the outer velocity U_e and the displacement thickness δ_1, are presented in Fig. 7.

From the mean streamwise velocity profile in Fig. 7a, it is seen that, for $y/\delta_1 > 1.0$, the LF-PIV and 2D-PIV results agree generally well. For the region $y/\delta_1 < 1.0$, in the displacement thickness, the profiles measured by the LF-PIV is less than satisfying. This region lies within several 3D interrogation regions of the wall in the LF-PIV experiment. There are two main reasons: on the one hand, due to the low speed of the inner boundary layer, the particles cannot easily enter the boundary layer, which will limit all PIV techniques including LF-PIV. The low particle density results in the low quality of reconstruction and less dominate cross-correlation peak. Specifically for LF-PIV, errors due to this cause are likely to be more significant in depth direction (z-direction) as the resolution is lower than the x- and y-direction and so, with less particles in this region, large errors in identification of the center of individual particles contribute more to the statistics. On the other hand, the DRT-MART method without volumetric calibration is sure to bring a large error to the reconstructed particles. The original DRT-MART method does not take the lens defects and misalignment between MLA and image sensor into account, which is the main source of false reconstruction. According to the most recent work (Shi et al. 2019), a volumetric calibration method for LF-PIV uses the point-like features in light-field particle images to precisely build the relation between voxels and their affected pixels. This calibration method can get a more accurate weighting coefficient for particle reconstruction, especially in regions further away from focal plane where the accuracy is significantly affected by optical distortions, and thus can substantially increase measurement accuracy. The effects of the erroneous reconstruction near the z-extremeties of the reconstructed volume can easily be seen in the averaged volumetric velocity field (Fig. 5c). In the z-direction, a variation of the mean streamwise velocity can be observed from the two-dimensional slices. This variation, which is larger than the uncertainty in the mean statistics, was caused by the erroneous reconstruction near the volume edges due to optical distortion.

For the Reynolds stress profiles plotted in Fig. 7b, c, the LF-PIV is able to observe some indication of the outer peak expected in the $\langle uu \rangle / U_e^2$ and $\langle vv \rangle / U_e^2$ profiles for APG-TBL flows and agree well with the 2D-PIV's result, where the peak location is near to the displacement thickness. The effective measurements extend down to approximately $y/\delta_1 = 0.2$ from the wall. The magnitude of the outer Reynolds stress peaks is measured as approximately $uu = 0.096 U_e^2$ and $vv = 0.0028 U_e^2$, comparing favorably to the Reynolds stress peak magnitudes suggested from the DNS and 2D-PIV results. Within the displacement thickness, the LF-PIV struggles to acquire accurate data, and at the upper edge of the measurement domain, the noise level of the measurement dominates and no freestream is observed. This is likely related to erroneous reconstruction by the DRT-MART reconstruction in the edge of the reconstructed volume.

The normalized Reynolds shear stress, $\langle uv \rangle / U_e^2$, profile is given in Fig. 7d. The location and magnitude of the peak at $1 < y/\delta_1 < 2$ agree with the 2D-PIV's result, but within one displacement thickness of the wall, the steep drop in the Reynolds shear stress magnitude obtained from LF-PIV relative to that measured by 2D-PIV is indicative of the LF-PIV's low resolution imposing a spatial filtering effect on the small-scale eddies near the wall.

In Fig. 7e, the $\langle ww \rangle / U_e^2$ normal component of Reynolds stress is shown as a function of wall-normal position. Since 2D-PIV does not yield the w-component of velocity, a comparison between the two methods cannot be made for this quantity. It is clear, however, that both the magnitude and double-peak shape of the $\langle ww \rangle / U_e^2$ profile observed in numerical studies of APG-TBLs (e.g., Kitsios et al. 2016) are not accurately recovered. This effect of the low (and varying) spatial resolution of LF-PIV in the viewing direction represents a severe limitation on the application of LF-PIV in its present state of development, at least when the viewing direction velocity component is of interest.

The LF-PIV is capable of providing an entire volumetric flow measurement from a single snapshot, similar to Tomo-PIV but with only a single camera. LF-PIV also differs from Tomo-PIV in that the resolution of the measurement inherently varies in the viewing axis direction (Shi et al. 2017). To demonstrate the measurement performance at different locations in the viewing (z-) direction, the Reynolds stress profile $\langle uu \rangle$ at two different z-positions is compared with 2D-PIV in Fig. 8. The slice of the velocity field in the focal plane ($z = 0$) is plotted in Fig. 8a, and the other slice ($z = 1.056$ mm, away from the camera focal plane) is shown in Fig. 8b. It is clear that LF-PIV performs well away from the focal plane, but struggles to accurately reproduce the results of the 2D-PIV at $z = 0$. The resolution of LF-PIV results varies in a complex manner in the z-direction. There are two major factors: on the one hand, the velocity field

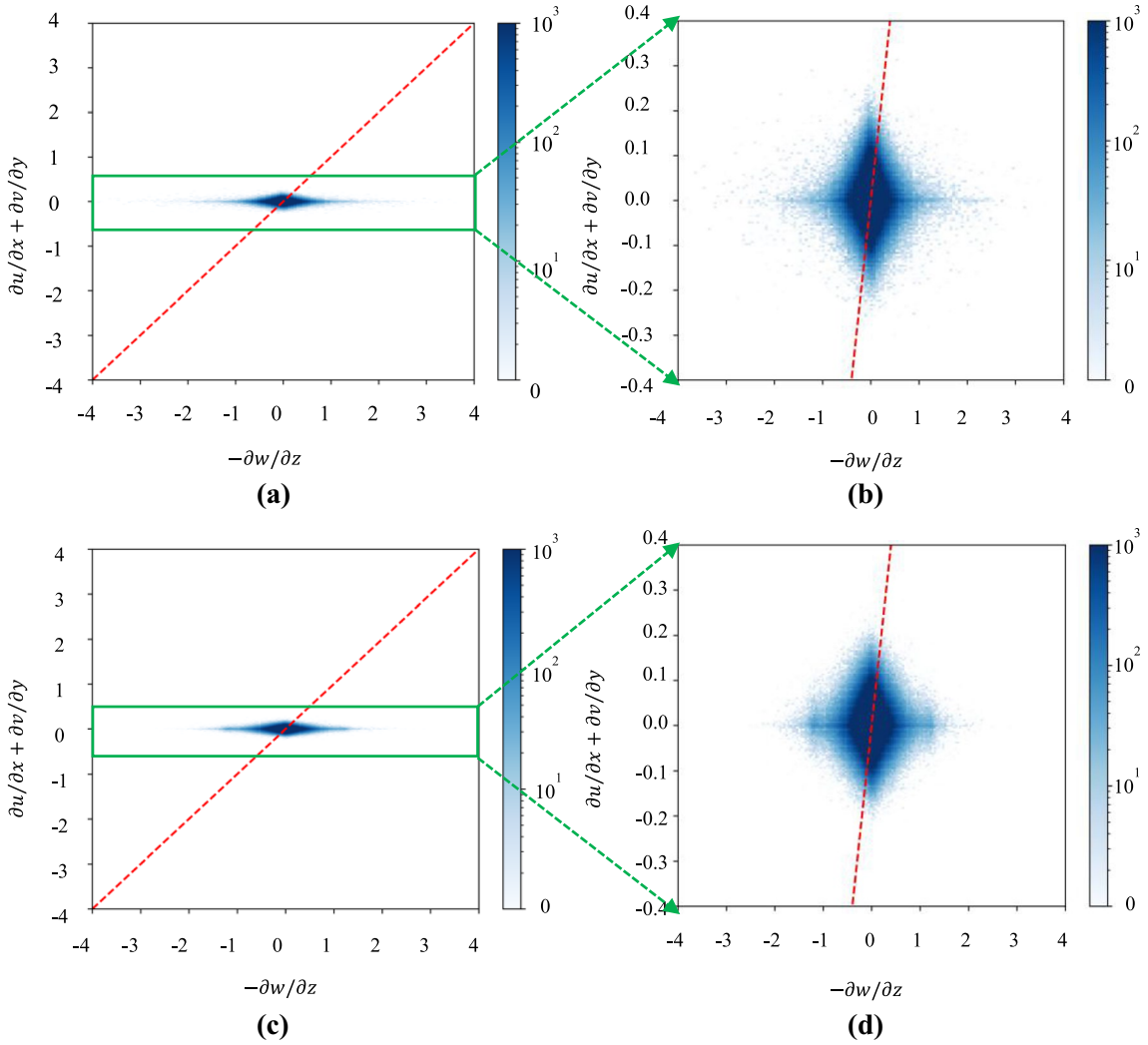

Fig. 6 **a** Divergence of velocity field in the outer layer test, **b** zoom in the green box area in **a**, **c** divergence of velocity field in the inner layer test, **d** zoom in the green box area in **c**; the red dash line is $-\partial w/\partial z = \partial u/\partial x + \partial v/\partial y$

generated by 3D cross correlation actually is using a thin volume's information. In this paper, with a final interrogation window size of $128 \times 128 \times 32$ voxels, the z-direction thickness of those related reconstructed voxels in cross correlation is around 1 mm. This will make the resolution of generated vector field in the z-direction not only depend on the exact slice resolution of the light-field camera. It is, somehow, a more averaged resolution of a thin volume than resolution of an isolated plane in exact depth. On the other hand, as what has been demonstrated in Shi et al. (2016) and Deem et al. (2016), the resolution of light-field camera has a complicated performance along the main optical axis (z-direction), which is the more fundamental reason pertinent to the physical law. The capability of the light-field camera to identify a simulated ideal point source light is changing in different positions away from the focal plane, which has been discussed in detail in the previous work (Shi et al. 2016). Also in Deem's work, a comparison between the central intensity profiles of the reconstructed particle and the actual simulated ideal particle location to illustrate the resolution of LF-PIV has been carefully made. In both works, there is a noticeable drop of the resolution near the focal plane, which can explain the large disparity between the LF and 2D-PIV result in Fig. 8a.

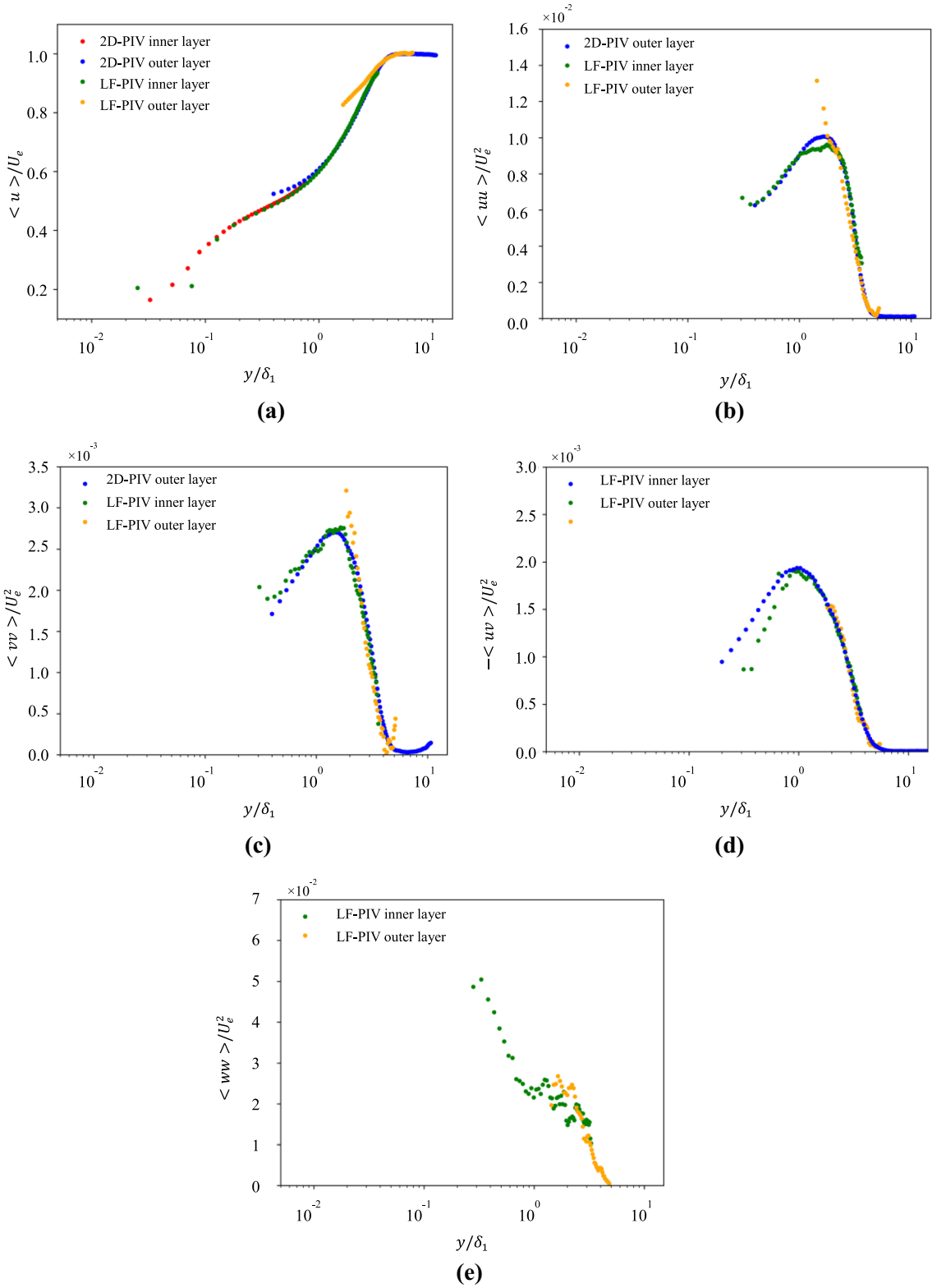

Fig. 7 Statistical profiles of the boundary layer computed from LF-PIV with measurements from 2D-PIV provided as a baseline for comparison. **a** Mean streamwise velocity; **b** streamwise component of the Reynolds normal stress $\langle uu \rangle$; **c** wall-normal component of the Reynolds normal stress $\langle vv \rangle$; **d** Reynolds shear stress $\langle uv \rangle$; **e** spanwise Reynolds normal stress $\langle ww \rangle$ obtained from LF-PIV only

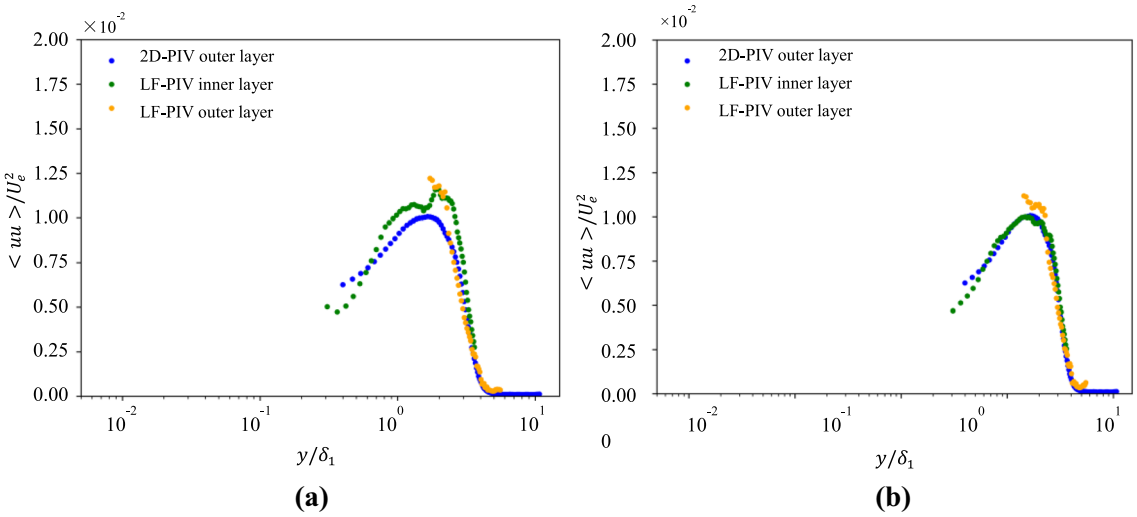

Fig. 8 Comparison of Reynolds stress profile $\langle uu \rangle$ of LF-PIV at different z-positions with 2D-PIV. Profiles are taken at **a** $z=0$ mm, and **b** $z=1.056$ mm, relative to the camera's focal plane ($z=0$ mm)

5 Conclusion

A self-similar APG-TBL is measured with the single-camera LF-PIV technique. Comparative analysis is made against results yielded by 2D-PIV measurements, demonstrating that reliable measurements could be obtained by LF-PIV of the mean streamwise velocity (in regions $y/\delta_1 > 0.1$) and Reynolds stress (in regions $y/\delta_1 > 0.2$). In addition, flow features in the depth direction can also be retrieved by the technique in a "snapshot" fashion, using only a single camera, a significant improvement in usability over the currently dominant 3D-3C measurement technique, Tomo-PIV. However, LF-PIV remains a maturing technology, and suffers from variation in resolution and accuracy in the viewing direction. Its measurement performance could be improved by increasing the MLA and sensor resolution. Meanwhile, with development of more robust light-field reconstruction and volumetric calibration algorithms, higher seeding density and optical distortion compensated reconstruction will further improve its measurement accuracy.

Acknowledgements Financial support provided by National Natural Science Foundation of China (Grant Nos. 11472175, 11772197).

References

Adrian RJ, Westerweel J (2011) Particle image velocimetry. Cambridge University Press, Cambridge

Atkinson C, Soria J (2009) An efficient simultaneous reconstruction technique for tomographic particle image velocimetry. Exp Fluids 47:553

Atkinson C, Buchner AJ, Kitsios V, Soria J (2015) A multi-camera PIV system for the study of self-similar APG turbulent boundary layers. In: 11th Int. Sym. on Particle Image Velocimetry -PIV15, September 14–16, Santa Barbara, California

Atkinson C, Buchner A-J, Sekimoto A, Kitsios V, Soria J (2016a) Experimental measurements of a self-similar adverse pressure gradient turbulent boundary layer. In: 20th Australasian Fluid Mechanics Conference, Perth, Australia

Atkinson C, Buchner A-J, Sekimoto A, Eisfelder M, Kitsios V, Soria J (2016b) Time-resolved piv measurements of a self-similar adverse pressure gradient turbulent boundary layer. In: The 18th international symposium on the application of laser and imaging techniques to fluid mechanics, Lisbon, Portugal

Belden J, Truscott TT, Axiak MC, Techet AH (2010) Three-dimensional synthetic aperture particle image velocimetry. Measure Sci Technol 21:125403

Bobke A, Vinuesa R, Örlü R, Schlatter P (2017) History effects and near equilibrium in adverse-pressure-gradient turbulent boundary layers. J Fluid Mech 820:667–692

Bolton JT, Thurow B, Arora N, Alvi F (2017) Single camera 3D measurement of a shock wave-turbulent boundary layer interaction. In: The 55th AIAA aerospace sciences meeting, Grapevine, Texas

Brucker C (1996) 3D scanning particle image velocimetry: technique and application to a spherical cap wake flow. Appl Sci Res 56:157–179

Buchner A-J, Lozano-Durán A, Kitsios V, Atkinson C, Soria J (2016) Local topology via the invariants of the velocity gradient tensor within vortex clusters and intense Reynolds stress structures in turbulent channel flow. J Phys Conf Ser 708:012005

Buchner A-J, Honnery D, Soria J (2017) Stability and three-dimensional evolution of a transitional dynamic stall vortex. J Fluid Mech 823:166–197

Chen H, Sick V (2017) Three-dimensional three-component air flow visualization in a steady-state engine flow bench using a plenoptic camera. SAE Int J Engines 10:625–635

Deem E, Zhang Y, Cattafesta L, Fahringer T, Thurow B (2016) On the resolution of plenoptic PIV. Measure Sci Technol 27:084003

Ding J, Wang J, Liu Y, Shi S (2015) Dense ray tracing based reconstruction algorithm for light-field volumetric particle image

velocimetry. In: 7th australian conference on laser diagnostics in fluid mechanics and combustion, Melbourne, Australia

Ding J, Lim D, Sheikh S, Xu S, Shi S, New TH (2018) Volumetric measurement of a supersonic jet with single-camera light-field PIV. In: The 18th international symposium on the application of laser and imaging techniques to fluid mechanics, Lisbon, Portugal

Eisfelder M P, Müller J S, Sekimoto A, Buchner A-J, Kitsios V, Atkinson C, Oberleithner K, Soria J (2018) Stability of a self-similar adverse pressure gradient turbulent boundary layer. In: 21st Australasian fluid mechanics conference, Adelaide, Australia

Elsinga G, Scarano F, Wieneke B et al (2006) Tomographic particle image velocimetry. Exp Fluids 41:933–947

Fahringer T, Lynch K, Thurow B (2015) Volumetric particle image velocimetry with a single plenoptic camera. Measure Sci Technol 26:115201

Herman GT, Lent A (1976) Iterative reconstruction algorithms. Comput Biol Med 6:273–294

Hinsch K (2002) Holographic particle image velocimetry. Measure Sci Technol 13:R61–R72

Katz J, Sheng J (2010) Applications of holography in fluid mechanics and particle dynamics. Annu Rev Fluid Mech 42:531–555

Kitsios V, Atkinson C, Sillero JA, Borrell G, Gungor AG, Jiménez J, Soria J (2016) Direct numerical simulation of a self-similar adverse pressure gradient turbulent boundary layer. Int J Heat Fluid Flow 61:129–136

Kitsios V, Sekimoto A, Atkinson C, Sillero JA, Borrell G, Gungor AG, Jiménez J, Soria J (2017) Direct numerical simulation of a self-similar adverse pressure gradient turbulent boundary layer at the verge of separation. J Fluid Mech 829:392–419

Li H, Ding J, Zhao Z, Qu W, Xiong J, Shi S (2017) Investigation of 3D flow behaviour inside a 3×3 rod bundle using Light Field-PIV and the matched refractive index techniques. In: The 12th international symposium on particle image velocimetry. Busan, Korea

Pereira F, Gharib M, Dabiri D et al (2000) Defocusing digital particle image velocimetry: a 3-component 3-dimensional DPIV measurement technique. Application to bubbly flows. Exp Fluids [Suppl.]:S78–S84

Prasad AK, Adrian RJ (1993) Stereoscopic particle image velocimetry applied to liquid flows. Exp Fluids 15:49–60

Scarano F (2013) Tomographic PIV: principles and practice. Meas Sci Technol 24:1–28

Sheskin D (2000) Handbook of parametric and nonparametric statistical procedures, 2nd edn. Chapman and Hall/CRC, London

Shi S, Wang J, Ding J, Zhao Z, New TH (2016) Parametric study on light field volumetric particle image velocimetry. Flow Measure Instrum 49:70–88

Shi S, Ding J, New TH, Soria J (2017) Light-field camera-based 3D volumetric particle image velocimetry with dense ray tracing reconstruction technique. Exp Fluids 58:78

Shi S, Ding J, Atkinson C, Soria J, New TH (2018) A detailed comparison of single-camera light-field PIV and tomographic PIV. Exp Fluids 59:46

Shi S, Ding J, New TH, Liu Y, Zhang H (2019) Volumetric calibration enhancements for single-camera light-field PIV. Exp Fluids 60(1):21

Soria J (1996) An investigation of the near wake of a circular cylinder using a video-based digital cross-correlation particle image velocimetry technique. Exp Thermal Fluid Sci 12(2):221–233

Vila CS, Örlü R, Vinuesa R, Schlatter P, Ianiro A, Discetti S (2017) Adverse-pressure-gradient effects on turbulent boundary layers: statistics and flow-field organization. Flow Turbul Combust 99:589–612

Willert C, Gharib M (1992) Three-dimensional particle imaging with a single camera. Exp Fluids 12:353–358

Xu S, Ding J, Zhao Z, Atkinson C, Soria J, Shi S (2017) 3D flow measurements of circular air jet at $\mathrm{Re}=30{,}000$ using light field particle image velocimetry. In: The 12th international symposium on particle image velocimetry, Busan, Korea

Zhao Z, Buchner A-J, Ding J, Shi S, Atkinson C, Soria J (2018) Volumetric measurements of a self-similar adverse pressure gradient turbulent boundary layer using single-camera light-field particle image velocimetry. In: The 18th international symposium on the application of laser and imaging techniques to fluid mechanics, Lisbon, Portugal